SUPPORTING INFORMATION

Outstanding Heat Loss via Nano-Octahedra above 20 nm in Size: From Wustite-rich Nanoparticles to Magnetite Single-Crystals.

Idoia Castellanos-Rubio[*], *Irati Rodrigo, Rahul Munshi, Oihane Arriortua, José S. Garitaonandia, Ana Martinez-Amesti, Fernando Plazaola, Iñaki Orue, Arnd Pralle, Maite Insausti*[*].

Table of contents (ESI†)

Model S1. Modelling single magnetic domain with thermal fluctuations. Fokker-Planck equation.

Magnetization of the single domain is represented by a vector of constant modulus (M) $\vec{M} = M\hat{r}$. The evolution of unit vector $\hat{r}$ with time is given by the dimensionless implicit Gilbert equation:

$$\frac{d\hat{r}}{d\ t} = \gamma\hat{r} \times \vec{B}_{e\ f\ f} \alpha\hat{r} \times \frac{d\hat{r}}{d\ t} \qquad (S1)$$

In this equation α is the so-called Gilbert damping constant (dimensionless constant), γ is the gyromagnetic ratio (taken as a positive number) and $\vec{B}_{e\ f\ f} = (-1/M)\partial\ V\partial\hat{r}$ ($\partial/\partial\hat{r} \equiv g\ r\ a)\ q$ is the effective magnetic field, which includes the any external applied field as well as any anisotropy field of magnetocrystalline, shape or dipolar origin, $V\ \hat{r}$) being the total energy density of the single domain. The dependence of $\hat{r}$ with time can be obtained explicitly after multiplying both sides of equation (S1) by ($\hat{r} \times$) operator and performing simple algebraic manipulations as:

$$\frac{d\hat{r}}{dt} = \frac{\gamma}{1+\alpha^2}\left(\hat{r} \times \vec{B}_{eff}\right) + \frac{\gamma\alpha}{1+\alpha^2}\left[\left(\hat{r} \times \vec{B}_{eff}\right) \times \hat{r}\right] \qquad (S2)$$

This is the explicit version of the dynamical equation that in the limit $\alpha \rightarrow 0$, becomes the earlier Laudau-Lifschizt equation. In (S2) the first term is responsible of the gyroscopic movement (rotation around $\vec{B}_{e\ f\ f}$) and the second one accounts for the gradual reorientation of $\vec{M}$ along $\vec{B}_{e\ f\ f}$ Given that $\vec{B}_{e\ f\ f} = (-1/M)\partial\ V\partial\hat{r}$, equation (S2) can be expressed as a function of energy density gradient as:

$$\frac{d\hat{r}}{dt} = -g'\left(\hat{r} \times \frac{\partial V}{\partial \hat{r}}\right) - h'\frac{\partial V}{\partial \hat{r}} \qquad S3)$$

This is so by considering that $\hat{r} \cdot \partial V/\partial \hat{r} = 0$. Here g' and h' are constants of movement defined as: $g' = \frac{\gamma}{M(1+\alpha^2)}$ and $h' = \frac{\gamma\,\alpha}{M(1+\alpha^2)}$. Considering the gyromagnetic ratio of free electron, magnetization M of magnetite and a Gilbert damping constant of 0.05, $g' \sim 360000 \cdot (m^3/asJ)$ and $h' \sim 18000 \cdot (m^3/asJ)$. In spherical coordinates, equation (S3) takes the following form:

$$\frac{d\hat{r}}{dt} = \left(\frac{g'}{sin\theta}\frac{\partial V}{\partial \varphi} - h'\frac{\partial V}{\partial \theta}\right)\hat{\theta} - \left(g'\frac{\partial V}{\partial \theta} + \frac{h'}{sin\theta}\frac{\partial V}{\partial \varphi}\right)\hat{\varphi} \qquad S4) \qquad ($$

This is a first order partial differential equation that can be solved by Runge-Kutta type algorithms. $V(\hat{r}, t)$ is the energy landscape of the problem. If thermal energy is taken into account, equation (S4) must be modified to include fluctuations of the magnetization.

Thermal fluctuations . In Stoner-Wohlfart Based Models, magnetization of the single domain is well determined by a single vector that is firmly anchored to the instantaneous energy minima. However, thermal effects should bring about certain "disorder" or "fluctuation" of the single domain magnetic dipole around equilibrium orientation. In such case, magnetization should be determined not with a single vector but with a probability distribution of orientations (or representative *state* points over the unit sphere) that will be referred as $W(\hat{r}, t)$. According to F.W. Brown's approach, magnetization dynamics can be understood as a current of representative points moving

around the surface of the unit sphere with number density $W(\hat{r}, t)$ and current density $\vec{J}(\hat{r}, t)$. These representative points cannot be created nor destroyed so W and $\vec{J}$ verify the continuity equation:

$$\partial W/\partial t = -\partial \vec{J}/\partial \hat{r} \qquad (\text{-odri } \vec{J}) \qquad S5) \qquad (\text{}$$

Brown postulates a diffusion contribution to the current density of the form $-k\,\partial W/\partial \hat{r}$ in such a way that current $\vec{J}$ is given by:

$$\vec{J} = W\frac{d\hat{r}}{d\,t} - k\frac{\partial W}{\partial \hat{r}} \qquad S6) \qquad (\text{}$$

Note that $\vec{J} = W\vec{v}$ in case of negligible thermal fluctuation and in this case W represents the probabilistic orientation of a large number of particles or equals the delta function for a single particle. Simply by substituting $d\hat{r}/d\,t$ from equation (S4) in equation (S6) the current density in spherical coordinates results in:

$$\vec{J} = -\left[\left(h\frac{\partial V}{\partial \theta} - \frac{g'\partial W}{sin\partial\theta\varphi}\right)W + k\frac{\partial W}{\partial \theta}\right]\hat{\theta} - \left[\left(g\frac{\partial V}{\partial \theta} + \frac{h'\partial W}{sin\partial\theta\varphi}\right)W + \frac{k'\partial W}{sin\partial\theta\varphi}\right]\hat{\varphi} \qquad S7)$$

Now it is enough to calculate the divergence of this current to obtain the evolution with time of the probability density W in equation (S1):

$$\frac{\partial W}{\partial t} = g\frac{\partial}{\partial \hat{r}}\left(W\hat{r}\times\frac{\partial W}{\partial \hat{r}}\right) + h\frac{\partial}{\partial \hat{r}}\left(W\frac{\partial W}{\partial \hat{r}}\right) + k\frac{\partial^2 W}{\partial \hat{r}^2} \qquad S8) \qquad (\text{}$$

Using very basic vector calculus rules involving *grad*, *div* and *curl*, and realizing that $div(\hat{r}\times grad\,g) = 0$, equation (S8) is easily transformed in :

$$\frac{\partial W}{\partial t} = g\hat{r}\left(\frac{\partial V}{\partial \hat{r}} \times \frac{\partial W}{\partial \hat{r}}\right) + h\frac{\partial}{\partial \hat{r}}\left(W\frac{\partial V}{\partial \hat{r}}\right) + k\frac{\partial^2 W}{\partial \hat{r}^2} \qquad (S9)$$

This is the Fokker-Planck equation ($\partial W/\partial t = L_{FP}W$) of the problem. In spherical coordinates equation (9) takes the following form:

$$\frac{\partial W}{\partial t} = \frac{g}{sin\theta}\left(\frac{\partial V}{\partial \theta}\frac{\partial W}{\partial \varphi} - \frac{\partial V}{\partial \varphi}\frac{\partial W}{\partial \theta}\right) + h\left(\frac{\partial V}{\partial \theta}\frac{\partial W}{\partial \theta} + \frac{1}{sin^2\theta}\frac{\partial V}{\partial \varphi}\frac{\partial W}{\partial \varphi}\right) + k\frac{\partial^2 W}{\partial \hat{r}^2} + h\,W\frac{\partial^2 V}{\partial \hat{r}^2} \qquad (S10)$$

Last term contains the Laplacian operator acting over W and V. From the point of view of numerical calculations, it is more convenient to work out directly with equations (S5) and (S6), in spherical coordinates:

$$\frac{\partial W}{\partial t} = \frac{1}{sin\theta}\frac{\partial}{\partial \theta}\left[(sin\theta)J_\theta\right] + \frac{1}{sin\theta}\frac{\partial}{\partial \theta}\left[J_\varphi\right] \qquad (S11)$$

By realizing that $\vec{J} = J_\theta\hat{\theta} + J_\varphi\hat{\varphi}$ is given in equation (S7). If one can assume that gradient of distribution W is parallel to gradient of energy ($\partial W/\partial \hat{r} \times \partial V/\partial \hat{r} = 0$) gyroscopic contribution can be dropped out from calculation.

Hydrodynamic-Size and Zeta-Potential

Table S1. Polydispersity index (PDI), mean hydrodynamic diameter (given in Intensity (Dh_I), Volume (Dh_V) and Number (DhN)) and Z potential (Pz) for samples with PMAO and PMAO-PEG coatings.

SAMPLE	COATING	PDI	D_{hI} (σ)(nm) [H_2O]	D_{hV} (σ)(nm) [H_2O]	D_{hN} (σ)(nm) [H_2O]	Pz (σ) (mV) [H_2O]
E	PMAO	0.27	149(7)	86(7)	65(5)	-34(0.1)
F		0.24	136(1)	87(6)	61(5)	-37(0.8)
G		0.24	184(2)	113(5)	78(5)	-31(0.5)
E	PMAO-PEG	0.16	180(11)	128(4)	99(8)	-13(0.3)
		PDI	**D_{hI} (σ)(nm) [PBS]**	**D_{hV} (σ)(nm) [PBS]**	**D_{hN} (σ)(nm) [PBS]**	
		0.14	198(1)	137(3)	104(5)	

As the packing factor for octahedral NPs in BCC or FCC is ~ 0.5, and the hydrodynamic diameter of samples E, F and G (taken in Intensity, Volume or Number) is below 200 nm, it can be concluded that the corresponding clusters are formed by just few tens of NPs.

On the other hand, samples with PMAO-PEG have a larger hydrodynamic diameter and a lower surface charge due to the PEG functionalization. These F-MNPs with PMAO-PEG coating are stable in physiological media.

Scherrer calculation

The crystalline sizes of Samples A-G have been calculated by the deconvolution of the (311) diffraction peak of magnetite and/or (200) diffraction peak of wüstite, using the Scherrer equation (S12):

$$D = \frac{K\lambda}{B_{estruc.}\cos\theta} = \qquad \text{(S12)}$$

Where K is the shape factor (0.9-0.95), $B_{structure}$ = $B_{observed}$-$B_{instrumental}$ is the full width at half maximum, λ is the X-ray wavelength (in our case = ($K\alpha_1$+$K\alpha_2$)/2=1.5418Å), and θ is the peak position.

Table S2. Parameters obtained from the deconvolution of (311) of magnetite or (200) of wüstite and crystalline size using Scherrer equation.

Sample	Diffraction peak	B obs. [°2θ]	B inst. [°2θ]	Peak pos. [°2θ]	B struct. [°2θ]	Crystalline size [nm]*
A	311	0.350	0.120	35.572	0.230	36(1)**
	200	0.500	0.120	42.429	0.380	22(1)
B	200	0.615	0.12	42.498	0.495	17(1)
C	200	0.872	0.120	42.763	0.752	11(1)
D	311	0.393	0.120	35.570	0.273	30(1)
	200	0.584	0.120	42.409	0.464	18(1)
E	311	0.359	0.120	35.619	0.239	35(1)
F	311	0.447	0.120	35.611	0.327	25(1)
G	311	0.301	0.120	35.595	0.181	47(2)

*Uncertainty of the calculated sizes is on the last significant digit.

**In sample A the dimension of the crystalline size obtained from 311 peak, corresponds to the diameter of a sphere that has the same volume as the shell of the core-shell NP.

Rietveld Refinements

The Rietveld analysis of the diffraction data of samples A-G was performed using the FULLPROF program and the fitted diffractograms and the corresponding parameters are shown in Table S3 and Figures S1, S2 and S3.

The line shape of the diffraction peaks was generated by a pseudo-Voigt function and the background interpolated between some fixed background points of the diagrams. In the final run the following parameters were refined: unit-cell parameters, zero-point, half-width, symmetry parameters, scale factor, atomic coordinates and thermal isotropic factors.

Table S3. Summary of crystallographic data and Rietveld refinement details for the samples A-G. $R_p = 100\sum|y_{oi} - y_{ci}|/\sum|y_{oi}|$ the pattern factor R-factor, $R_{wp} = 100\{\sum w_i(y_{oi} - y_{ci})^2 / \sum w_i(y_{oi})^2\}^{1/2}$ the weighted pattern R-factor, $R_{exp} = 100\{(N - P + C)^2 / \sum w_i(y_{oi})^2\}^{1/2}$ the expected pattern R factor, $R_B = 100\sum|I_{obs} - I_{calc}|/\sum I_{obs}$ Bragg factor, $\chi^2 = 1/N\sum_i(y_{ci} - y_{oi})^2/\sigma^2(y_{oi})^2$ where y_{oi} is the observed intensity at the *i*th step, y_{ci} is the calculated intensity, w_i is the weighting factor, N total number of data points 'observations', P is the number of parameters adjusted and C the number of constraints applied.

Sample	**E**	**G**	**F**	**A**	**D**	**C**	**B**
Space Group	F d-3m	F d-3m	F d-3m	F d-3m	F d-3m	F d-3m	F d-3m
a = b = c	8.381(3)	8.3869(5)	8.384(5)	8.386(3)	8.394(7)	8.401(2)	8.417(4)
V (Å3)	588.72(4)	589.73(5)	589.28(6)	589.8184)	591.49(8)	592.9(2)	596.3(5)
% Fe_3O_4	100*	100	100	88.2	74.1	76.6	71
S.G.				F m-3m	F m-3m	F m-3m	F m-3m
A = b				4.262(5)	4.266(2)	4.219(6)	4.25183)
V(Å3)				77.44(2)	77.643(7)	75.15(2)	76.82(1)
% FeO				11.7*	25.9	23.4	29*
R_p	10.6	12.3	14.8	10.7	10.5	9.3	9.89
R_{wp}	13.8	15.8	18.5	13.5	13.1	11.9	13.0
R_e	8.3	8.8	9.8	10.17	10.46	10.20	10.75
χ^2	2.7	3.2	3.5	1.76	1.57	1.37	1.46
R_B	12.3	10.3	13.7	14.5 / 23.7	18.6 (20.8)	18.0 (11.5)	14.2(8.6)

**These percentages are in agreement with the ones determined by Mossbauer spectroscopy and displayed in Table 2 of the main paper.*

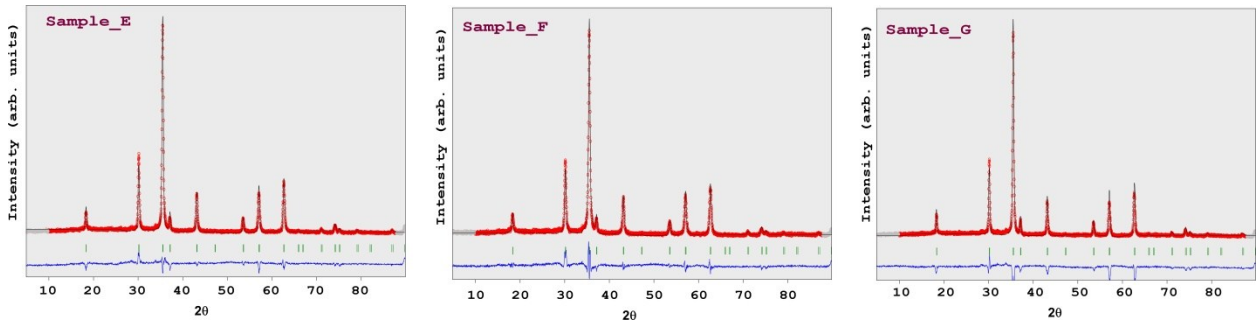

Figure S1. Rietveld refinements for sample E, F and G. The experimental diffractogram is represented with red dots, the calculated one with a black line and the difference between them in blue. Samples E, F and G are just formed of magnetite phase.

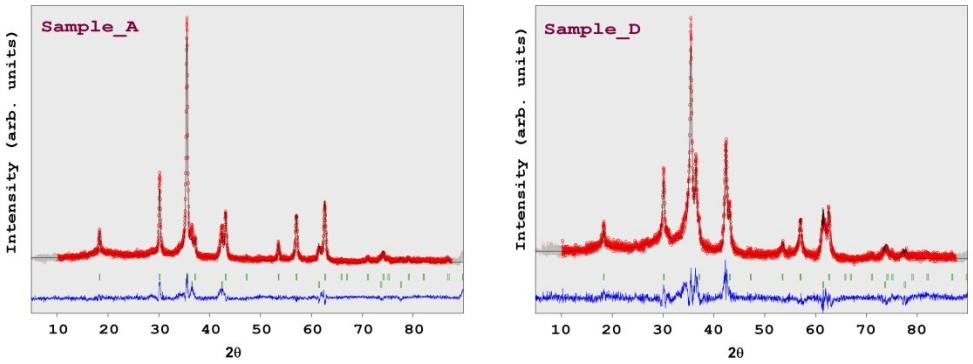

Figure S2. Rietveld refinements for sample A and D. The experimental diffractogram is represented with red dots, the calculated one with a black line and the difference between them in blue. Samples A and D present a mixture of magnetite and wüstite phases.

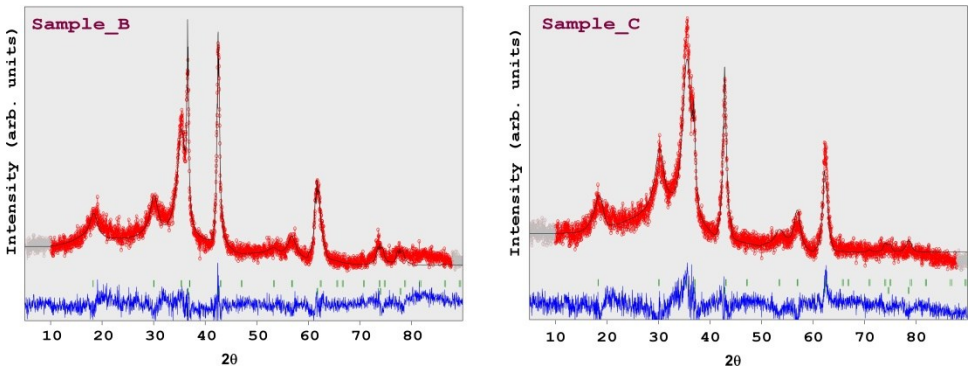

Figure S3. Rietveld refinements for sample B and C. The experimental diffractogram is represented with red dots, the calculated one with a black line and the difference between them in blue. Samples B and C present a mixture of magnetite and wüstite phases and poor crystallinity.

Thermogravimetric measurements

The thermogravimetric measurements of samples A-F are displayed in Figure S1.

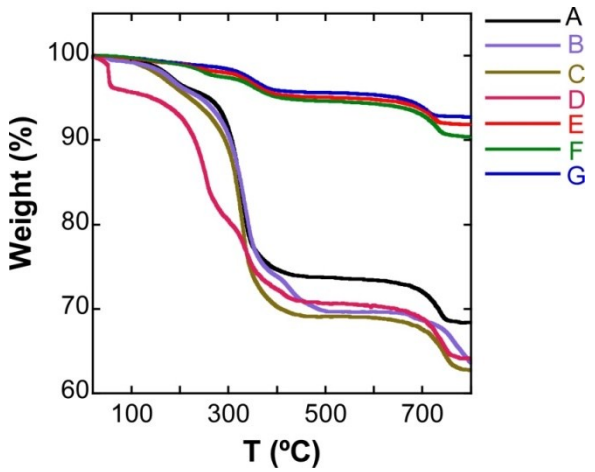

Figure S4. Thermogravimetric measurement of samples A-G in powder.

The organic matter percentage determined by thermogravimetry in as-synthesized NPs is summarized in Table S1.

Table S4. Summary of the organic matter percentage (O.M. %) in samples A-G.

Sample	A	B	C	D	E	F	G
O.M. (%)	31.7	36.5	37.5	35.5	8.2	9.7	7.2

Zero Field Cooling-Field Cooling measurements.

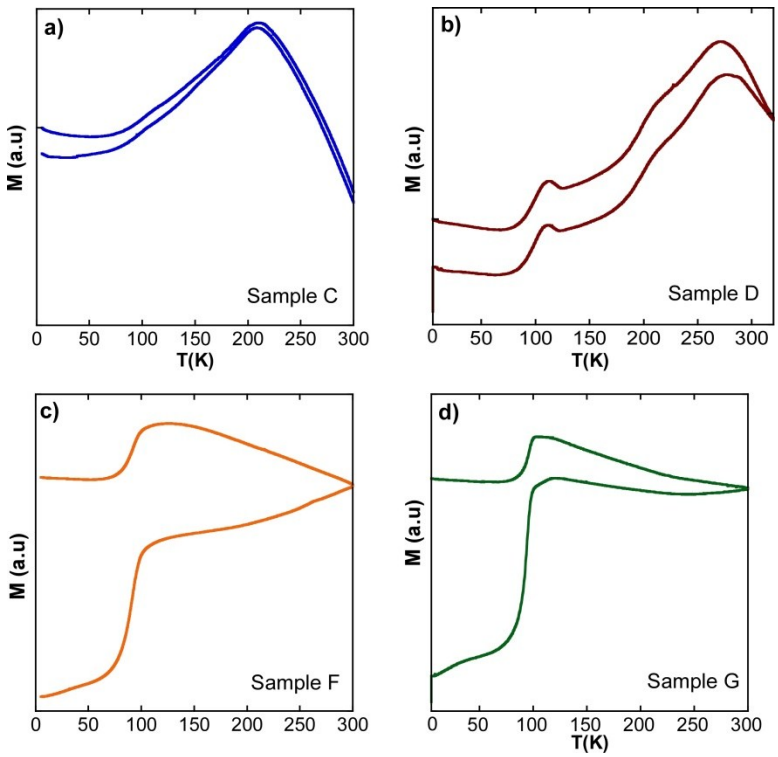

Figure S5. ZFC-FC curves obtained at a constant field of 1 mT: **a)** sample C, **b)** Sample D, **c)** Sample F and **d)** Sample G.

ZFC/FC curves of octahedral and single phase magnetite particles of samples F and G show the strong jump at the Verwey temperature transition point (~100 K). In contrast, more heterogeneous samples C and D only display traces of it.

Quasi-static magnetic measurements. Hysteresis loops of sample E, F and G

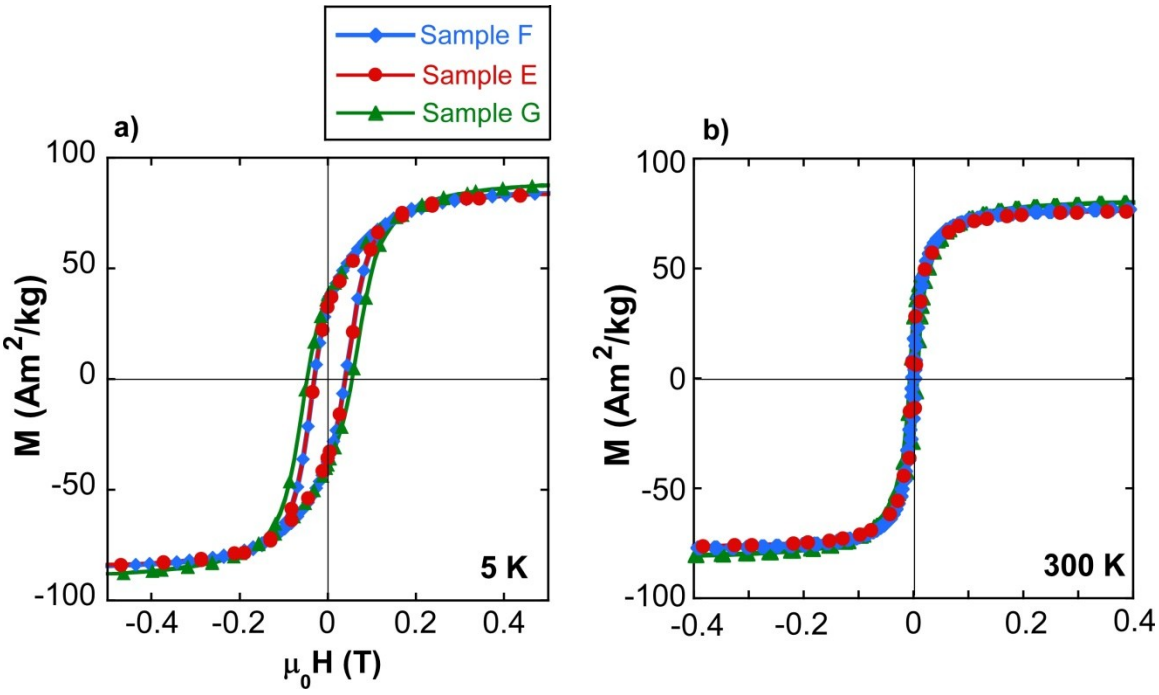

Figure S6. Hysteresis loops of samples F, E and G at **a)** 5 K and **b)** 300 K.

Hysteresis loops at 5K of samples E, F and G look very similar. Actually, only that of sample G is slightly wider than the other two, which are superimposed to each other. In all cases reduced remanence is around 0.44 and coercive fields are 43, 43 and 54 mT respectively.

Table S4. Saturation magnetization values of samples E, F and G at 5 K and 300 K.

	Sample E	**Sample F**	**Sample G**
Ms (Am^2/kg) **at 5 K**	86	87	91
Ms (Am^2/kg) **at 300 K**	77	78	82

Dynamical Hysteresis loops as a function of the excitation frequency

Figure S4 shows how the SAR of the samples E, F and G is mostly independent of the excitation frequency.

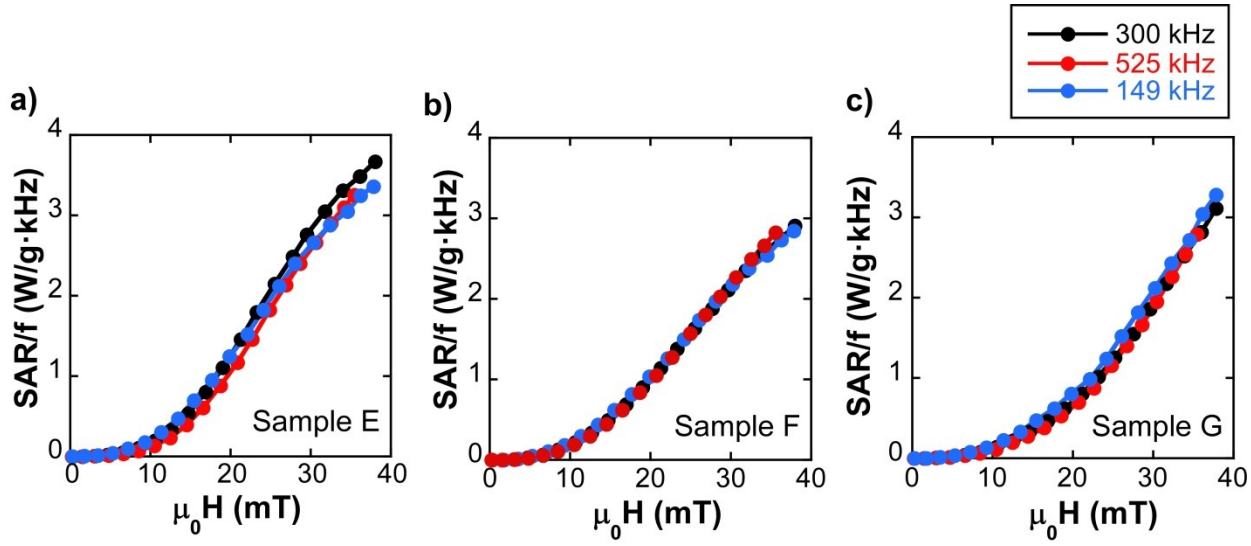

Figure S7. Experimental SAR normalized by frequency (SAR/f in W/g•kHz) as a function of the magnetic field amplitude at different excitation frequencies of 300, 525 and 149 kHz for **a)** Sample E, **b)** Sample F and **c)** Sample G.

Normalized SAR displayed in Figure S4 for octahedral particles E, F and G merge in a single curve. According to the relationship between SAR and hysteresis area, given by:

$$SAR(W/g) = \frac{f}{c}A = \frac{f}{c}\oint \mu_0 M_t dH_t \qquad (S13)$$

Normalized SAR (SAR/f) becomes exactly the normalized hysteresis area of the dynamical loops. In consequence, the area is basically frequency-independent, as deduced from Figure S4 and this is a characteristic of Stoner-Wohlfart Based Models or, conversely, of the high energy barrier approximation to the problem of thermal fluctuation of magnetic single domains.

Modelling the AC magnetic response: the role of dipolar interactions

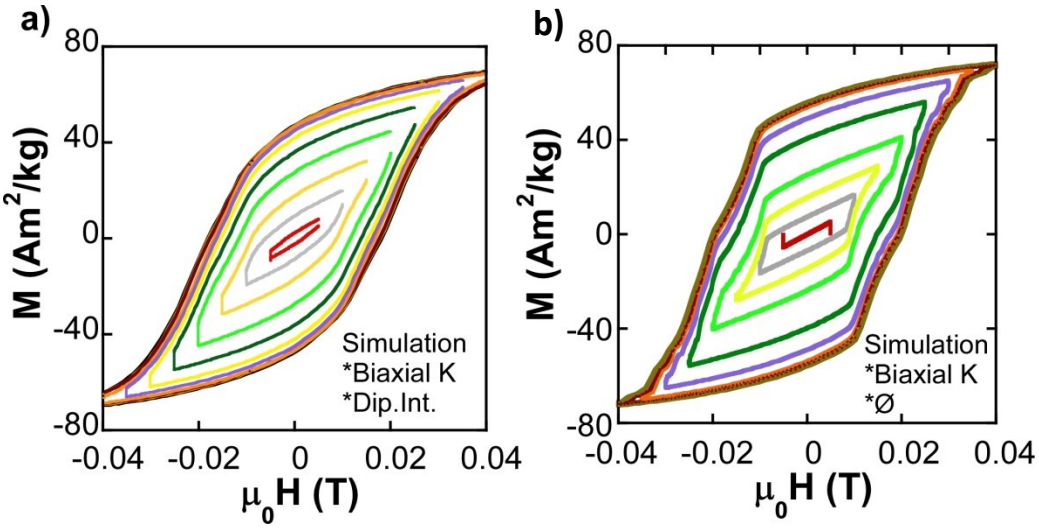

Figure S8. Calculated hysteresis loops by solving LLG equation for particles of 35 nm with biaxial anisotropy **a)** Interacting NPs in a BCC-type arrangement (Figure 9h of the main paper) and **b)** Non-interacting NPs. In both cases biaxial anisotropy is determined by constants Kx=16 kJ/m^3 and Ky=13 kJ/m^3. Magnetocrystalline contribution is considered as equal to that of pure magnetite (11 kJ/m3)

In Figure S5, hysteresis loop simulations for sample E, shown in manuscript and performed by constructing a BCC-type cluster (a) are compared with those obtained after switching off dipolar interactions, so corresponding to a single particle model (b). It is observed that remanence is a bit higher in the single particle limit and hysteresis exhibits some kinks that are absent when dipolar interactions are taken into account.

Colloidal stability of sample E with PMAO-PEG coating

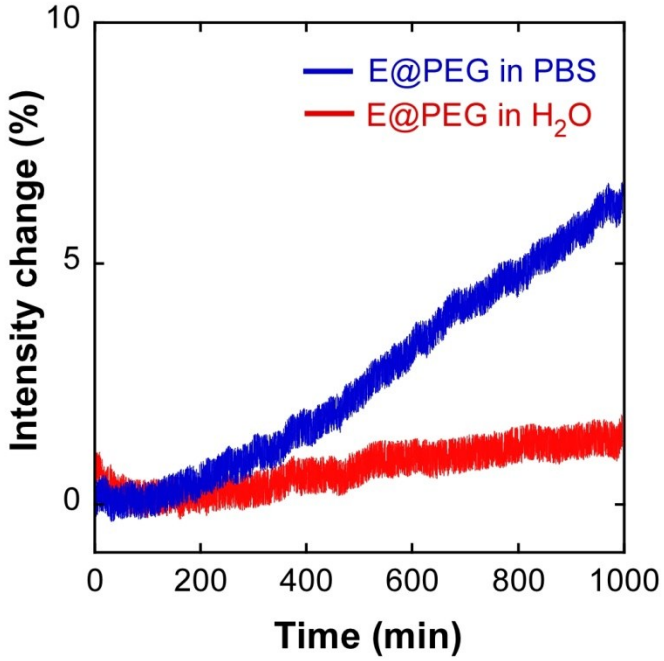

Figure S9. Transmitted light intensity through E@PEG colloidal sample in D.I. water (red curve) and phosphate-buffered saline (PBS: 1x, pH=7.4) (blue curve) is represented as a function of time.

In this experiment, the light intensity is expected to increase as colloidal particles start depositing on the bottom of the glass column. Water dispersed NPs are extremely stable during almost 1 day while PBS dispersed NPs show a slight tendency to sedimentation (< 5% of the total sample) in the same time-scale. Note in any case that this sedimentation takes place very slowly so that it is undetectable during the first 3-4 hours.

TEM micrograph of sample E@PMAO-PEG

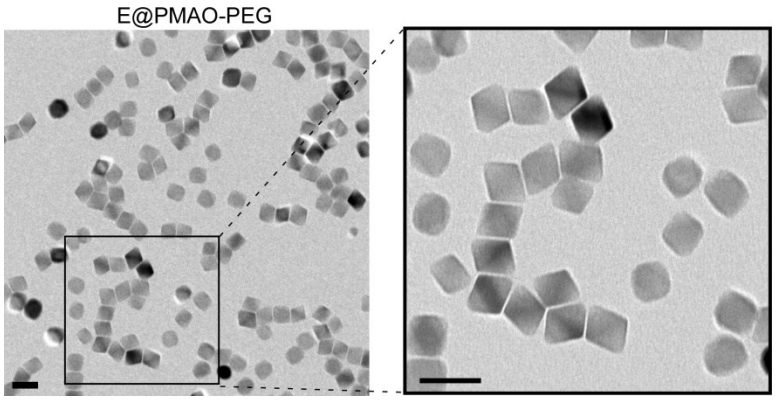

Figure S10. TEM micrographs of sample E@PMAO-PEG showing small clusters and chains of few nanoparticles. Scale bars 50 nm.

AC hysteresis simulation of BCC, FCC clusters and short chains

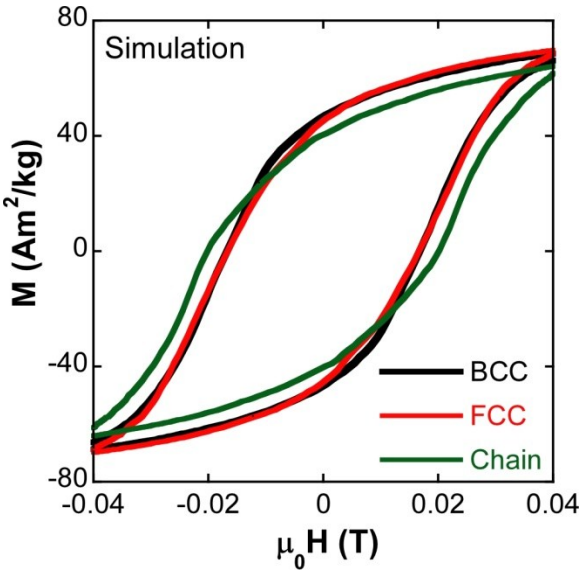

Figure S11. AC hysteresis loops similations for a BCC, FCC clusters of around 20 particles and chain configurations of 8 particles. Simulations have been done assuming that M=420 kA/m, α=0.05, f=300 kHz.

Simulations of Figure S6 have been done with formally the same energy density function given by:

$$V = \sum_{i}^{N}\left[V_{i}^{cubic} - K_1\alpha_x^i - K_2\alpha_z^i - \mu_0 MH(\hat{u}_H \cdot \hat{r}_i) + \sum_{j\neq i}^{N} -\frac{\mu_o M^2 v}{4\pi r d_{ij}^3}\left[3(\hat{r}_i \cdot \hat{a}_{ij})(\hat{r}_j \cdot \hat{a}_{ij}) - (\hat{r}_i \cdot \hat{r}_j)\right]\right] (S14)$$

Summation term inside large bracket, differs from BCC to FCC cluster. For simulations we fix $K_1 = 13.5\ kJ/m^3$ and $K_2 = 16\ kJ/m^3$, M=420 kA/m and v to the volume corresponding to particles with equivalent sphere diameter of 30 nm. Figure S7 illustrates the effect of different clustering on the hysteresis losses of magnetic nanoparticles under AC magnetic excitations. Simulation performed with BCC and FCC type clusters becomes quite indistinguishable and only slight changes are observed for the case chain-type assembling.